WILEY-VCH

DOI: 10.1002/ ((please add manuscript number))

Article type: Full Paper

Fabrication of N-doped graphene-carbon nanotube hybrids from Prussian blue for Lithium-sulfur Batteries

Dawei Su, Michael Cortie, and Guoxiu Wang *

Dr. Dawei Su, Prof. Guoxiu Wang

Centre for Clean Energy Technology, Faculty of Science, University of Technology Sydney, NSW 2007, Australia.

Prof. Michael Cortie

Institute for Nanoscale Technology, Faculty of Science, University of Technology Sydney, NSW 2007, Australia.

E-mail: Guoxiu.Wang@uts.edu.au

ABSTRACT: Hybrid nano-structures containing one-dimensional (1D) carbon nanotubes and two-dimensional (2D) graphene sheets have many promising applications due to their unique physical and chemical properties. Herein, we found Prussian blue (dehydrated sodium ferrocyanide) can be converted to N-doped graphene-carbon nanotube hybrid materials through a simple one-step pyrolysis process. Through FESEM, TEM, XRD, Raman spectra, AFM, and isothermal analyses, we identified that 2D graphene and 1D carbon nanotubes were bonded seamlessly during the growth stage. When used as the sulfur scaffold for lithium-sulfur batteries, it demonstrated outstanding electrochemical performance, including a high reversible capacity (1221 mA h g^{-1} at 0.2 C rate), excellent rate capability (458 and 220 mA h g^{-1} at 5 C and 10 C rates, respectively), and excellent cycling stability (321 and 164 mA h g^{-1} at 5 and 10 C (1 C = 1673 mA g^{-1}) after 1000 cycles). The enhancement of electrochemical performance can be attributed to the three-dimensional architecture of the hybrid material, in which, additionally, the nitrogen doping generates defects and active sites for improved interfacial adsorption. Furthermore, the nitrogen doping enables the effective trapping of lithium

polysulfides on electroactive sites within the cathode, leading to a much improved cycling performance. Therefore, the hybrid material functions as a redox shuttle to catenate and bind polysulfides, and convert them to insoluble lithium sulfide during reduction. The strategy reported in this paper could open a new avenue for low cost synthesis of N-doped graphene - carbon nanotube hybrid materials for high performance lithium-sulfur batteries.

Keywords: One step synthesis, nitrogen-doped graphene - carbon nanotube hybrid materials, lithium-sulphur batteries

Introduction

Because of the high theoretical capacity (1673 mA h g^{-1}) and energy density (2600 W h kg^{-1}) of sulfur, lithium-sulfur (Li-S) batteries can, in principle, boost capacity five-fold over the current lithium-ion batteries. Furthermore, sulfur is a naturally abundant element (around 3 % of the Earth's mass), has a low cost, and is environmentally benign. Therefore, increasing number of the research groups focus on the Li-S batteries. However, practical applications of Li-S batteries are currently hindered by several obstacles. Sulfur is an insulator, which causes poor electrochemical contact within the electrode material. The intermediate polysulfide products can be dissolved in the electrolyte, and they can shuttle between the anode and cathode. This causes the so-called 'shuttling effect' which is associated with an irreversible loss of sulfur, resulting in low Coulombic efficiency, low cycling capacity, and an increase in internal resistance. Furthermore, the final insoluble product Li_2S always induces large volume expansion due to the differences in densities of Li_2S (1.66 g cm^{-3}) and sulfur (2.03 g cm^{-3}), leading to a rapid capacity decay.[1]

So far, many efforts have been made to improve the performance of Li-S batteries. The most popular approach is to encapsulate sulfur in the pores of carbon materials or a conductive polymer matrix. An encouraging early indication is that, in some cases, the special structure of sulfur carriers such as porous carbon can prevent polysulfides from dissolving in the electrolyte.[2] Macroporous or

mesoporous carbon materials have useful large pore volumes but their large pores have proved to be inefficient for the capture of sulfur and, furthermore, they do not block the naturally high solubility of polysulfides.[1b] Microporous carbon materials with pore sizes < ~1 nm, on the other hand, can effectively increase the electrochemical performance of Li-S batteries.[3] (The IUPAC Gold Book[4] recommends the term 'microporous' for carbonaceous materials with pore sizes < 2 nm. They are also commonly described as 'nanoporous' in the literature).

Carbon nanotubes (CNTs), a 1-D allotrope of carbon with extraordinary properties, have been widely investigated in recent decades. Not only do CNTs exhibit outstanding mechanical strength and a very large surface-to-volume ratio, some specific forms are also highly electrically conductive. For this latter reason, CNTs have been used to construct electrochemical electrodes for sensing[5] and energy storage.[6] Graphene is a recently discovered 2-D sp^2 carbon, which exhibits an even higher charge-carrier mobility and specific surface area than CNTs. Graphene is also an attractive choice for potential applications in actuators,[7] solar cells,[8] supercapacitors,[9] and batteries.[10] Multi-walled carbon nanotubes,[11] graphene,[12] graphene oxide[13] have been trialed for the Li-S batteries also. Qian Sun *et al.* reported an aligned and laminated sulfur-absorbed mesoporous carbon/CNT hybrid for Li-S batteries with a high capacity of 1226 mA h g^{-1} and achieves a capacity retention of 75% after 100 cycles at 0.1 C.[14] However, both forms of CNT and graphene exhibit a tendency to aggregate due to strong van der Waals interactions. This degrades the attainable physical properties of carbon nanotubes and graphene. The synthesis of CNT and graphene composites with a 3D hierarchical structure can effectively mitigate the self-aggregation and re-stacking of carbon nanotubes and graphene, thereby preserving their intrinsic physical properties. Theoretical research has also suggested that a covalently bonded graphene and single-walled carbon nanotube hybrid material can extend their electronic properties to 3D for applications in energy storage and nanoelectronic technologies.[15] Therefore, 3D carbon-networks combining 1D carbon nanotubes and 2D graphene

have attracted considerable interest for the Li-S batteries.[16] Huisheng Peng *et al.* summarized recent progress on hybrid carbon structures for the rechargeable Li-S batteries.[17]

Generally, hybrids of CNTs and graphene can be synthesized by catalytic growth of one building block on the other one.[18] Such as Qiang Zhang and co-authors fabricated graphene/single-walled carbon nanotube hybrid by a catalytic growth on layered double hydroxide at a high temperature over 950 °C as cathode materials for Li-S batteries. The hybrid exhibited good performance with a capacity as high as 650 mA h g^{-1} after 100 cycles even at a high current rate.[19] However, the stability of metal catalysts on carbon supports is very complicated.[18] Some recent attempts have been made to fabricate carbon nanotube and graphene hybrid films by spin-coating homogeneously mixed solutions of the two carbon-based nanomaterials.[20] However, the hybrid films consist of aggregated thick graphene layers with poor controllability. There are also reports of hydrothermal processes using graphene oxide (GO) and oxidized multi-walled carbon nanotube as precursors to synthesize carbon nanotube and graphene composites.[21] So far, however, reports of hybrids in which integration of high-quality aligned carbon nanotube and graphene have been achieved are very rare. Generally, it seems that the excellent physical properties of the pure CNT and graphene allotropes are not inherited by the hybrid structure.[16a]

It has been further reported that, tunable chemical techniques, such as using functional groups, doping, and surface modification on the sp^2 carbon, can help with the attainment of the desired physical and chemical properties. For example, in energy storage applications, it was found that nitrogen doped sp^2 carbons have significantly improved electrochemical performance and catalytic activity.[10a] This is because nitrogen bears five valence electrons which induce a shift in the Fermi level to the conducting band.[22] When nitrogen-doped graphene and carbon nanotube (N-GE-CNTs) hybrids were used as cathode materials for Li-S batteries, enhanced cycling and rate performances can be demonstrated.[23] Therefore, N-GE-CNTs hybrids are also a promising candidate for Li-S batteries. Previously, the nitrogen was doped in from outside sources, such as ammonia,[21] pyridine,[24]

or melamine.[25] For example, Cheng Tang *et al.* used the ammonia to introduce nitrogen atoms into the carbon framework to synthesize the nitrogen-doped aligned carbon nanotube/graphene sandwich via a two-step CVD growth method, which demonstrated the enhanced cyclic and rate performances (1152 mA h g^{-1} at 1 C, maintaining ca. 880 mA h g^{-1} after 80 cycles).[18]

Here we report a facile one-step method to synthesize Fe_3C@N-GE-CNTs hybrids from the low-cost raw material Prussian blue. It was observed that graphene and CNTs were bonded seamlessly during the growth stage, forming a 3D nano-architecture. When the as-prepared Fe_3C@N-GE-CNTs hybrids were used as a 3D scaffold to accommodate sulfur in Li-S batteries, a high reversible capacity of 1221 mA h g^{-1} was achieved. Excellent cycling stability was attained, with fading rates of 0.015% and 0.025 % per cycle at 5 C and 10 C rates over 1000 cycles, respectively. The enhancement of electrochemical performances can be attributed to the 3D N-GE-CNTs hybrid nano-architecture with improved electrical conductivity. Furthermore, the nitrogen doping can induce more defects and active sites in the carbon framework and effectively trap lithium polysulfides at electroactive sites within the cathode.

Experimental

Synthesis of Fe_3C@N-GE-CNTs hybrids. Anhydrous $Na_4Fe(CN)_6$ was obtained by dehydration of commercial $Na_4Fe(CN)_6 \cdot 10H_2O$ (Sigma-Aldrich, ≥ 99 %) at 150 °C for 24 hours. Dehydrated $Na_4Fe(CN)_6$ was annealed at 900 °C for 3 hours with a heat up rate of 5 °C min^{-1} to convert it to the hybrid material. After cooling to the room temperature, the final product was obtained. To analyze the formation mechanism of Fe_3C@N-GE-CNTs hybrids, the dehydrated $Na_4Fe(CN)_6$ was annealed at 850, 950, and 1000 °C in the N_2 atmosphere.

Synthesis of S@Fe_xS@N-GE-CNTs hybrids. We used the melt-diffusion strategy to load S.[26] In a typical process, 25 wt. % Fe_3C@N-GE-CNTs hybrids and 75 wt. % sulfur were ground together. Then, the mixture was put into a glass tube sealed with plastic wrap and heated to 155 °C. The mix-

ture was maintained at this temperature overnight. For the comparison experiments, appropriate S was also melted with trigonal $Na_4Fe(CN)_6$ and RGO-CNTs composites.

Structural and physical characterization. The phase and crystal structure of the material were characterized by X-ray diffraction (XRD, Siemens D5000) using Cu K_α radiation with a scanning step of 0.01° s^{-1}. The morphology of the material was observed by field emission scanning electron microscopy (FESEM, Zeiss Supra 55VP). The details of the material and crystal structure were analyzed by transmission electron microscopy (TEM) and high-resolution TEM (HRTEM, JEOL JEM-2011). Selected area electron diffraction (SAED) patterns were recorded by a Gatan charge-coupled device (CCD) camera in a digital format. Elemental mapping was obtained by energy dispersive X-ray spectroscopy (Bruker SDD EDS Quantax 400 system). Thermo-gravimetric/differential thermal analysis (TG/DTA) was performed at a heating rate of 5 °C min^{-1} under air flow from room temperature to 900 °C with a 2960 SDT system (Lukens Drive New Castle, DE 19720). The thickness of graphene nanosheets was measured by atomic force microscopy (AFM) using a Bruker Dimension 3100 instrument under a MicroMasch NSC16 tip with 40 N m^{-1} of spring constant. The AFM sample was deposited on the mica plate for AFM measurement. Raman spectra were measured using a Renishaw inVia Raman spectrometer system (Gloucestershire, UK) equipped with a Leica DML Bmicroscope (Wetzlar, Germany) and a 17 mW at 633 nm Renishaw helium neon laser source. X-ray photoelectron spectroscopy (XPS) measurements were carried out on a Kratos XSAM-800 spectrometer with an Mg K_a radiation source.

Electrochemical testing. The electrodes were prepared by first blending 80 wt. % as-prepared composite materials, 10 wt.% acetylene carbon black, and 10 wt. % poly(vinylidene fluoride) binder (PVDF, $(CH_2CF_2)_n$, Sigma-Aldrich) in N-methyl-2-pyrrolidone (NMP, C_5H_9NO, Sigma-Aldrich, 99.5 %) to form a slurry, and the slurry was then pasted onto aluminum foil and dried in a vacuum oven for 12 h, which was followed by pressing at 200 kg cm^{-2}. The mass loading of each electrode was approximately 1.1 mg cm^{-1}. Electrochemical measurements were carried out using CR2032 coin

cells with lithium foil as reference and counter electrode and a porous polypropylene (Celgard 2300) as the separator. The CR2032 coin cells were assembled in an argon-filled glove box (UniLab, Mbraun, Germany) with low levels of H_2O and O_2 (H_2O < 0.01 ppm, O_2 < 0.01 ppm). The electrolyte solution was 1 M LiTFSI and 1 wt. % $LiNO_3$ in 1, 3-dioxolane and 1, 2-dimethoxyethane (volume ratio 1:1). The galvanostatic charge-discharge measurements were performed at room temperature at different current densities in the voltage range from 1.7 to 2.7 V. Cyclic voltammetry (CV) was carried out on a CHI 660C electrochemistry workstation with a scan rate of 0.1 mV s^{-1} from 1.7 to 2.7 V.

Computational methods. Thermodynamic calculations were carried out with ThermoCalc v3.1 using the TCFE7 database to calculate the equilibrium phases resulting when molten S with Fe_3C@N-GE-CNTs hybrids at 155 °C.

Results and discussion

The synthesis process for the Fe_3C@N-GE-CNTs hybrid is illustrated in **Figure 1**a. The anhydrous $Na_4Fe(CN)_6$ nanocrystals were simply obtained by dehydration of commercial $Na_4Fe(CN)_6{\cdot}10H_2O$ (space group: P21/n (14), a = 9.766 Å, b = 11.44 Å, c = 9.029 Å, and β = 97.48°, **Figure 1**b. The SEM, TEM, and HRTEM images of $Na_4Fe(CN)_6$ are shown in **Figure S1** (Supplementary Information, SI). **Figure 1**a also shows the crystal structure of $Na_4Fe(CN)_6{\cdot}10H_2O$, $Na_4Fe(CN)_6$ and Fe_3C. As revealed by the TGA measurement (**Figure S2**, SI), the commercial $Na_4Fe(CN)_6{\cdot}10H_2O$ can be completely dehydrated at 150 °C, with 37.2 % weight loss. The XRD patterns of the anhydrous $Na_4Fe(CN)_6$ are shown in **Figure 1**c. All the diffraction peaks match JCPDS No. 00-001-1026 and are consistent with previously reported results.[27] The structure was Rietveld refined to be trigonal symmetry (space group: P-3, (147), **Figure 1**a) with satisfied convergence factors (R_{wp} = 12.7 %, R_p = 9.73 %). As indicated by the diffraction peak in the low d-spacing range (2θ = 15.2°), the obtained trigonal $Na_4Fe(CN)_6$ has a large amount of intercalation space in the crystal structure (d =

5.73 Å). As shown in **Figure S3** (SI), the refined lattice of the as-prepared trigonal $Na_4Fe(CN)_6$ consists of the trigonal layers formed by the $[Fe(CN)_6]^{4-}$ complexes. After annealing at 900 °C for 3 hours in nitrogen atmosphere, the XRD patterns can be refined to the Fe_3C (**Figure 1**d), with a orthorhombic symmetry (space group: Pnma (62), a = 5.098 Å, b = 6.807 Å, and c = 4.528 Å, R_{wp} = 13.3 %, R_p = 7.56 %). The field emission scanning electron microscopy (FESEM) image (**Figure 1**e) revealed that the annealed products have a typical hierarchical structure, consisting of graphene nanosheets and carbon nanotubes, as illustrated in **Figure 1**a. The free standing graphene, atomically thin, can be observed in **Figure 1**f and g. The carbon nanotubes have a diameter of around 100 nm (**Figure 1**h). **Figure 1**i shows a carbon nanotube connected to a graphene layer with junctions. Meanwhile, Fe_3C nanoparticles can be observed on the tips of the carbon nanotubes. Obviously, Fe_3C functions as the catalyst to grow carbon nanotubes, as indeed is widely used in the chemical vapor deposition method[28] and consistent with previous reports.[29] As illustrated in **Figure 1**j, the carbon nanotube appears to replicate the shape of the Fe_3C catalyst on the graphene substrate. The carbon network expands by lifting off from the catalyst particle, which itself is thereby restructured. It was found that the crystal structure of the precursor is crucial for the synthesis of the 3D Fe_3C@N-GE-CNTs nano - architecture. When the fcc cubic structure of annealed $Na_4Fe(CN)_6$ nanocrystals (space group: $F\bar{4}3m$ (216), a = 9.96 Å) was combined with graphene oxide for synthesis via a low-temperature hydrothermal method (**Figure S4** and **S5**, SI), there is no carbon nanotube formation in the final carbon materials (**Figure S6**, SI). Similar results have been reported previously.[30] When the cubic structure Prussian blue precursor is pyrolyzed, a core-shell carbon can be obtained instead of the graphene and carbon nanotube hybrid structure. It can be hypothesized that the anhydrous $Na_4Fe(CN)_6$ precursor presents much larger interstitial sites with a 5.73 Å interlayer distance. There is no direct chemical bond between the adjacent $[Fe(CN)_6]^{4-}$ octahedral complexes, allowing the evaporation of sodium ions and formation of Fe_3C. Consequently, the growth of carbon nanotubes is fostered. Furthermore, the annealing temperature is another factor for the final product's architec-

ture. As shown in **Figure S7** (SI), at 850 °C, there are no carbon nanotubes formed (**Figure S7**a, SI) because the temperature is not high enough for triggering the growth of carbon nanotubes. When the temperature was raised to 900 °C, the carbon nanotubes grew with the ~ 30 % relative amount (**Figure S7**b, SI). Increasing the annealing temperature to 950 °C, more carbon nanotubes grew from the Fe_3C catalysts, forming carbon nanotubes with larger diameters with the ~ 45 % relative amount (**Figure S7**c, SI). When the temperature was increased to 1000 °C, no remaining graphene nanosheets can be observed. Instead, much larger carbon nanotubes with ~ 95 % relative amount or even core-shell structures Fe_3C@C were formed (**Figure S7**d, SI). Therefore, we conclude that 900 °C is the optimal temperature for the growth of 3D Fe_3C@N-GE-CNTs hybrids. We conducted the TGA analysis of Fe_3C@N-GE-CNTs to figure out the amount of Fe_3C in the final hybrid structure is ~ 28 % (**Figure S8,** SI).

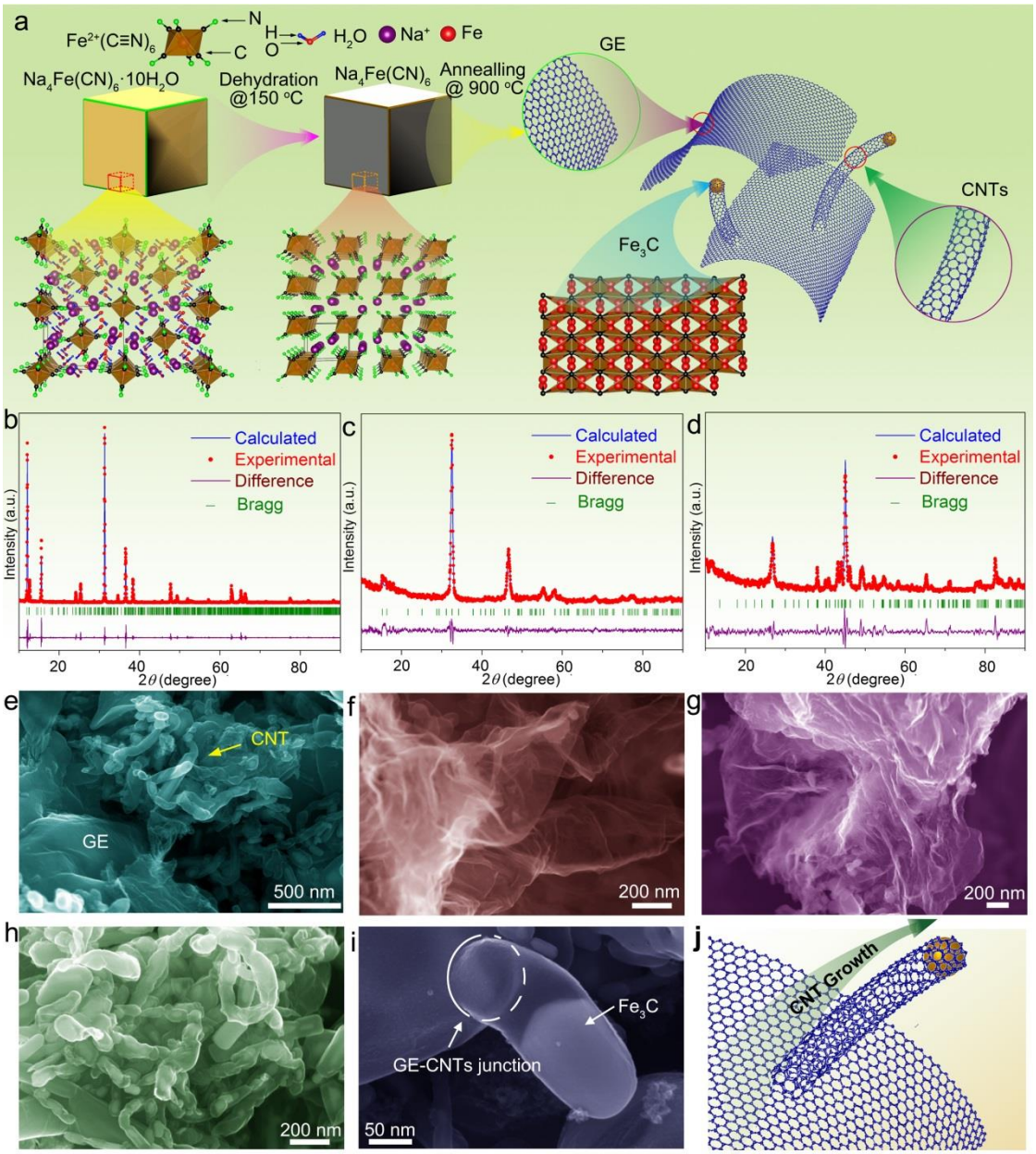

Figure 1. a. Illustration of synthesis process for the Fe_3C@N-GE-CNTs hybrids. b. Rietveld refinement pattern of X-ray diffraction data for commercial $Na_4Fe(CN)_6\cdot 10H_2O$ (b), anhydrous $Na_4Fe(CN)_6$ (c), and Fe_3C@N-GE-CNTs hybrids (d). The observed and calculated intensities are represented by the red circles and the blue solid line, respectively. The bottom purple-colored line shows the fitting residual difference. The Bragg positions are represented by light-green ticks. (e) – (i). FESEM images of Fe_3C@N-GE-CNTs hybrids. (j). Illustration of carbon nanotubes grown from graphene.

Figure 2a is a transmission electron microscopy (TEM) image of the graphene. A typical crumpled surface is clearly observed, indicating the features of the 2D structure. The high-resolution TEM (HRTEM) image (**Figure 2**b) shows that the material is slightly different from single-layer graphene. Several layers can be observed, which was confirmed by the AFM measurement (**Figure 2**c, top) together with their thickness profiles (**Figure 2**c, bottom). The height profile along the white line indicates it has ~ 13 nm thickness. As shown in **Figure 2**d, the carbon nanotubes force graphene towards the Fe_3C catalyst cluster. We used the high resolution TEM images to reveal the conjunction between CNTs and graphene layers. As shown in **Figure 2**e and **Figure S9**a (SI), the carbon nanotube root (light purple area in **Figure 2**e and mark in **Figure S**9a, SI) connect to the graphene plane (light yellow area in **Figure 2**e and mark in **Figure S9**a, SI) and orient towards the Fe_3C catalyst (light green area in **Figure 2**e and mark in **Figure S**9a, SI, the (210) crystal plane of Fe_3C with 2.38 Å d-spacing can be readily observed). The ring-like area, as marked by light pink color in **Figure 2**e is a characteristic property of covalent bonds between CNTs and graphene.[16a] Furthermore, from the typical carbon nanotube TEM image (**Figure 2**g), it can be seen that one tip of the CNT is open-ended. This is agreeing with the theoretical prediction that the CNT should be open-ended when it forms covalent bonds with the graphene basal layer,[31] and consisted with the previous reported covalent bonded CNT and graphene.[16a] Furthermore, as shown in **Figure S9**a (SI), the catalytic nanocrystal Fe_3C has the steps with 3-4 monolayers in height (as marked by arrows in the **Figure S9b**, SI) and the carbon layers emerge at various angles along with the steps and terminate at the stepped Fe_3C surface. Subsequent CNT layers nucleate at an already-grown Fe_3C-C interface as demonstrated by the corresponding crystal model (**Figure S9**c, SI). This suggests that the carbon layers will nucleate along with the surface of the catalytic centers (Fe_3C) and will form the catalyst-carbon (Fe_3C-C) interface and then get the growth of the CNT. Therefore, the carbon source has interactions with the catalytic centers during the growth of CNTs. Furthermore, such C-stabilized Fe_3C step-edges involves diffusion of C atoms toward and Fe_3C

atoms away from the graphitic layer-Fe_3C interface,[31c, 32] resulting the elongation of the Fe_3C catalyst crystal (**Figure 2**d). This dynamics of the catalytic Fe_3C crystal reshaping are critical for the alignment of the graphitic layers into a straight CNT (**Figure 2**d and f, The inner diameter of ~50 nm depends on the size of Fe_3C nanocrystal and the thickness of the CNT (~ 15 nm) is consistent with the graphene thickness). If the Fe_3C particle elongation is followed by an abrupt contraction, a bamboo-structured CNT will be created, with a conformal carbon overcoat behind (**Figure 2**g). Obviously, carbon activity drives the dynamic restructuring of the catalyst, which determines structural selectivity. When catalyst particle elongation is suppressed and encapsulated by carbon, resulting into the interruption of the Fe_3C-C interaction, CNT growth will be ceased (**Figure 2**h, The CNT has the typical 3.39 Å interlayer distance). On the basis of these observations, a possible mechanism shown in **Figure 2**i-l summarizes the different Fe_3C@N-GE-CNTs hybrids growth stages. At low temperature (850 °C), the sodium ions evaporate along the large interstitial spaces of the trigonal $Na_4Fe(CN)_6$ precursor (**Figure 2**i). When the temperature reaches 900 °C, the graphitic lattice starts to nucleate on the Fe_3C catalyst surface (**Figure 2**j). Initially, the carbon cap appears to replicate the shape of the apex of the Fe_3C particle (**Figure 2**j). It was reported that step sites on the catalyst surface nucleate the graphitic lattice formation[32] and that the carbon cap of a CNT is stabilized by the fact that carbon precipitation is faster than the speed of step withdrawal. After then, the carbon network expands by lifting off from the catalyst particle, which itself is thereby restructured (**Figure 2**k). Along with carbon nanotubes growth process, the growing nanotube forces its shape onto the Fe_3C particle, whereby constrains the Fe_3C particle to a more cylindrical shape (**Figure 2**l). When the tangential graphitic lattice encapsulates the catalyst particle, CNT growth will be terminated.[33]

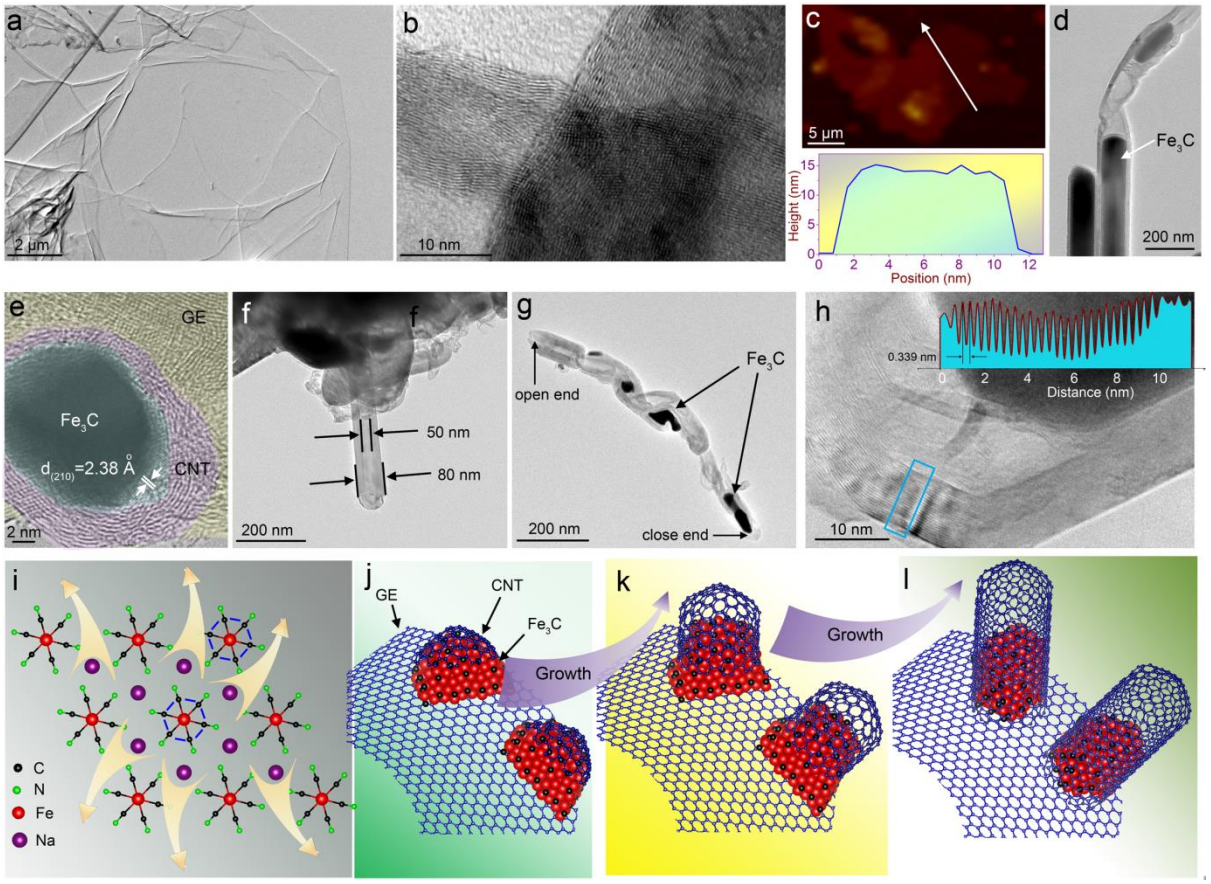

Figure 2. a. TEM image of graphene. b. HRTEM image of graphene. c. AFM measurement and thickness profiles. D. TEM image of carbon nanotube. e. HRTEM image of Fe_3C@N-GE-CNTs hybrids, which shows the conjunction of Fe_3C, carbon nanotube, and graphene. f. TEM image of root area of carbon nanotube growing on the graphene. g. TEM image of a typical carbon nanotube. h. HRTEM image of carbon nanotube. Inset is the thickness profile of the carbon nanotube wall. i-l. Schematic diagram of evolution of Fe_3C@N-GE-CNTs hybrids.

Figure 3a is the Raman spectrum of Fe_3C@N-GE-CNTs, which displays the well-defined D and G bands at 1328 and 1580 cm^{-1}, respectively, originating from a hybridized vibrational mode associated with graphene edges and the E_{2g} vibration of the sp^2-bonded carbon atoms, respectively. The intensity ratio of I_D/I_G is ~ 0.93, indicating edge defects in the graphene structure and a relatively low degree of graphitization.[34] The broad and asymmetric 2D peak at 2700 cm^{-1} implies that the sample

mainly consists of inhomogeneous multi-layer graphene sheets rather than single-layer graphene,[34] which is consistent with the TEM and AFM observations. Furthermore, based on the isothermal curve (**Figure 3**b) and pore size distribution (inset in **Figure 3**b), the as-prepared Fe_3C@N-GE-CNTs hybrids show a high BET surface area of 248 $m^2 g^{-1}$ and a high pore volume of 0.45 $cm^3 g^{-1}$. As compared, we also measured the surface area and pore volume of the reduced graphene oxide (rGO)-CNT to be 178 $m^2 g^{-1}$ and 0.21 $cm^3 g^{-1}$, respectively. Obviously, the N-GE-CNT hybrid structure exhibits the higher BET surface area, indicating the carbon nanotubes within N-GE-CNT hybrid can effectively brace graphene nanosheet to form the 3D hierarchical structure and mitigate the self-aggregation and re-stacking of nanocarbon materials. The XPS survey spectra (**Figure 3**c and d) shows the dominant C 1s peak at ca. 284.5 eV (**Figure 3**c) and the N 1s peak at ca. 399.9 eV (**Figure 3**d). The high-resolution XPS spectrum of C 1s (**Figure 3**c) can be deconvoluted into four peaks at 284.5, 285.7, 287.3 and 290.1 eV, which correspond to C–C, C=N (N–sp^2 C), C–N (N-sp^3 C) and O-C=O bonds,[35] respectively. The high-resolution XPS N 1s peak (**Figure 3**d) reveals the presence of pyridnic N (398.7 eV), pyrrolic N (399.9 eV) and graphitic N (401.2 eV),[35-36] as demonstrated by **Figure 3**e. The high intensity of graphitic N indicates the success of nitrogen doping in the Fe_3C@N-GE-CNTs hybrids. Furthermore, the EDS spectrum of the Fe_3C@N-GE-CNTs hybrids shows the K_α signal of N element (at ~ 0.392 KeV, **Figure 3**f), confirming the nitrogen dopant. By comparison, the Na element in the $Na_4Fe(CN)_6$ precursor has been completely removed after annealing at 900 °C for 3 hours (**Figure 3**f). The as-prepared Fe_3C@N-GE-CNTs hybrids were further characterized by EDS mapping and the uniform C, N, and Fe elements distribution is shown in **Figure S10** (SI).

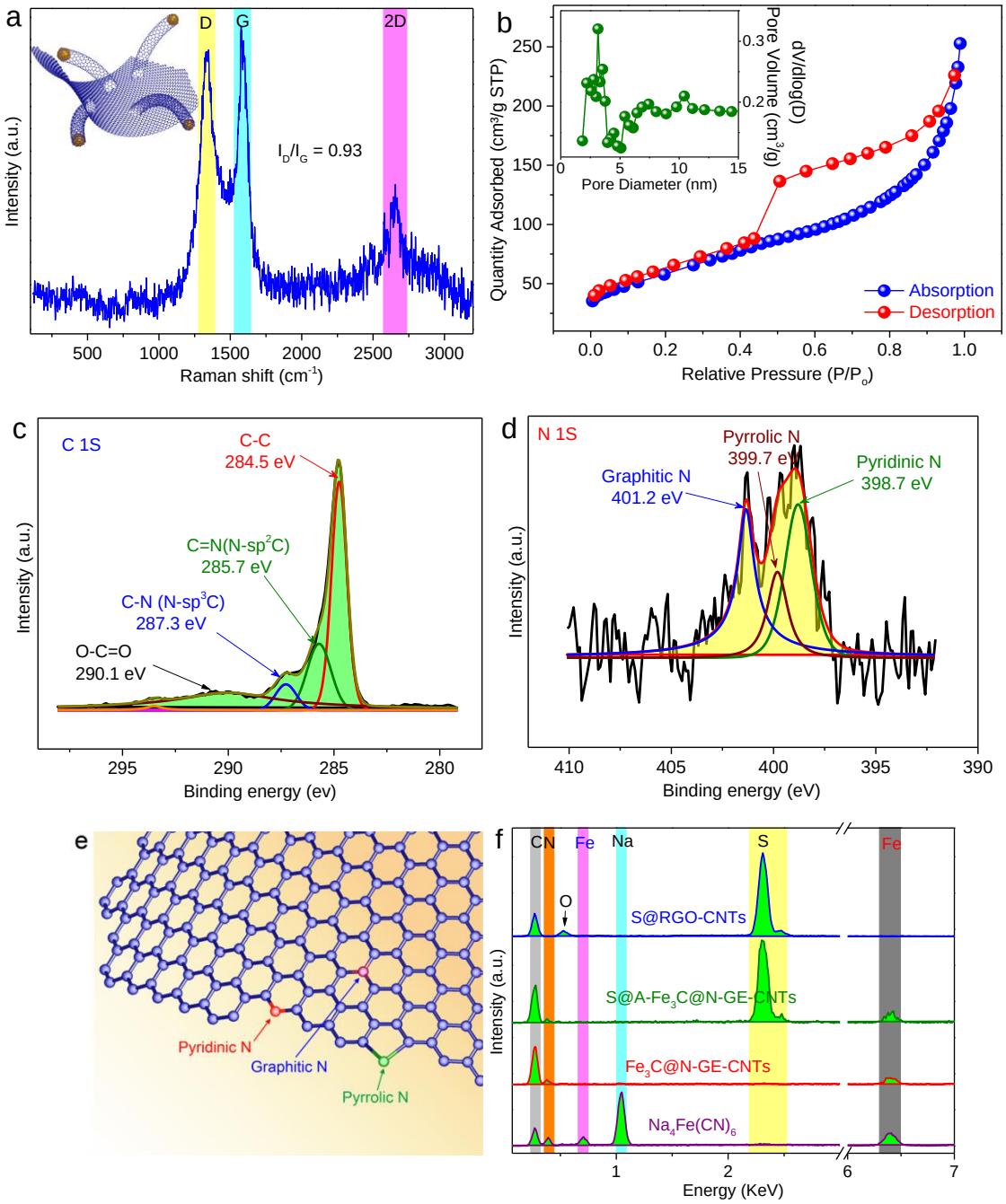

Figure 3. (a) Raman spectrum (b) isotherm analysis (inset shows pore size distribution.) (c) High-resolution C1s XPS spectra (d) N 1s XPS spectra (e) schematic diagram of N-doped graphene (f) EDS spectra of anhydrous $Na_4Fe(CN)_6$, Fe_3C@N-GE-CNTs hybrids, S@ Fe_3C@N-GE-CNTs hybrids, and S@RGO-CNTs composites.

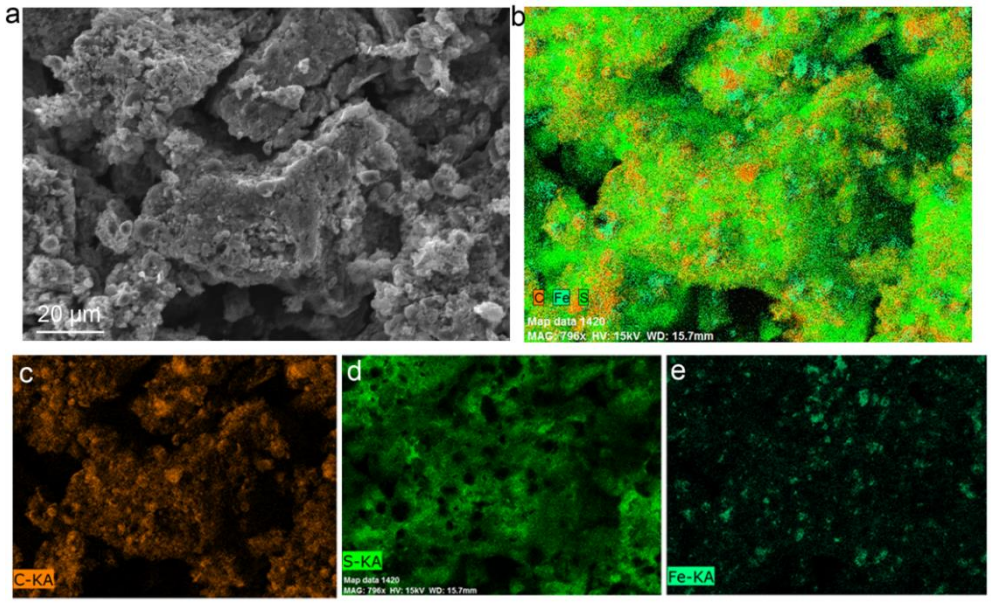

Figure 4. (a) FESEM image of sulfur loaded Fe_3C@N-GE-CNTs hybrids (b) EDS spectrum mapping, (c) uniform C elemental distribution, (d) S elemental distribution, (e) Fe elemental distribution.

As characterized above, the as-prepared Fe_3C@N-GE-CNTs hybrids present a 3D hierarchical structure, consisting of 2D graphene and 1D carbon nanotubes - but retaining the essential characteristics of each - which can effectively mitigate the self-aggregation and re-stacking of nanocarbon materials. Furthermore, the nitrogen dopant with five valence electrons induces a shift in the Fermi level to the conducting band, leading to an improved reactivity for Li-S batteries. For testing the electrochemical performance of Fe_3C@N-GE-CNTs hybrids in Li-S batteries, S was loaded by melt-diffusion method.[26] The FESEM images of S@Fe_3C@N-GE-CNTs hybrids are shown in **Figure 4**. No large bulk S aggregations can be found in the composite. Uniform C, S, and Fe elemental distributions can be observed using EDS spectrum mapping (green curve in **Figure 3**f, **Figure S11** (SI) and **Figure 4**). The high surface area and large pore volume of Fe_3C@N-GE-CNTs hybrids can accommodate the melted S. 2D graphene nanosheets can encase the S and 1D carbon nanotubes can work as a string to hold the graphene wrappers together, as indicated schematically in **Figure 5**a. After melting S with the as-prepared Fe_3C@N-GE-CNTs hybrids at 155 °C for 12 hours, the XRD pat-

terns of the mixture (blue curve in **Figure 5**b) can be indexed to crystalline S (JCPDS File No. 00-008-0247). Compared with the main peaks area of Fe_3C (at 40° - 50°), the XRD peaks corresponding to the Fe_3C (green curve in **Figure 5**b) noticeably disappeared, suggesting that Fe_3C lost its crystalline nature. Furthermore, no new XRD patterns can be observed except for S. Calculations made using Thermocalc™ indicated that the equilibrium phases resulting when molten S at 155 °C is reacted with Fe_3C are S, Fe_xS (pyrrhotite) and graphite. The XRD peaks for the pyrrhotite formed here are, however, either obscured by those of the S or it is poorly crystalline. The Raman spectrum of melted S with Fe_xS@N-GE-CNTs hybrids is shown in **Figure 5**c (blue curve). Besides the D, G and 2D bonds, corresponding to the N-GE-CNTs hybrids, there are new peaks at 149, 216, 245, 434, and 472 cm^{-1}, corresponding to the S_8,[37] as compared with the Raman spectrum of pure S (red curve in **Figure 5**c). Since a lack of XRD peaks indicates that the pyrrhotite was formed after melting with S, XPS was used to identify the chemical bonds. **Figure 5**d compares the binding energy measurement of Fe 2p of Fe_3C@N-GE-CNTs and after melting with S. Both of them exhibit two strong peaks, but with different positions. For the Fe_3C@N-GE-CNTs hybrids, the observed binding energy of Fe2p at 711.7 eV and 725.1 eV are attributed to the Fe 2p3/2 and Fe 2p1/2, respectively, which demonstrates the formation of Fe_3C. After melting with S, the binding energy at around 708.7 eV is attributed to Fe(III)-S and is always observed at the initial mackinawite surface.[38] **Figure 5**e shows the XPS of S 2p of the as-prepared material after melting with S. The observed peak of approximately 163.4 eV corresponds to the S^0 2p1/2, while the peak at around 162 eV can be ascribed to S^{2-} 2p1/2, which corresponds to the FeS.[39] The peaks at 165.4, 168.3 and 169.5 eV should be ascribed to the SO_4^{2-}, which originates from the surface oxy-groups on N-GE-CNT. Therefore, it is confirmed that, after melting with S, the hybrid materials are Fe_xS@N-GE-CNTs. The weight percentage of S was around 73 %, as measured by TGA (blue curve in **Figure 5**d). For comparison, RGO-CNTs composites were also tested. Due to the trigonal structure, $Na_4Fe(CN)_6$ has large interstitial sites with 5.73 Å interlayer distance. Therefore, trigonal $Na_4Fe(CN)_6$ can directly act as a carrier for the small sulfur mole-

cules. About 85 % S was loaded into the trigonal $Na_4Fe(CN)_6$, as revealed by the TGA (**Figure S12**, SI). Interestingly, S was evaporated at different temperatures in different matrixes (228, 230, 275, and 295 °C for the Fe_xS@N-GE-CNTs hybrids, RGO-CNTs composites, trigonal $Na_4Fe(CN)_6$, and bare S respectively) as revealed by the differentiated TGA curves (Figure S11, SI). This indicates the activity of different matrices for S-bonding. Obviously, Fe_xS@N-GE-CNTs hybrids show the highest activity for S due to the lowest evaporation temperature.

The electrochemical performance of the S@Fe_xS@N-GE-CNTs hybrids for Li-S batteries was firstly evaluated by cyclic voltammetry (CV, **Figure 6**a). The cells exhibited the typical electrochemical behavior of a sulfur cathode. Two obvious cathodic peaks at 2.35 and 2.03 V can be identified, corresponding to the transformation of cyclooctasulfur to long-chain lithium polysulfides (Li_2S_n, $n \geq 4$) and the decomposition of those polysulfides to short-chain lithium sulfides (Li_2S_n, $1 < n < 4$),[40] respectively. In the anodic scan, a prominent peak appeared at 2.37 V, corresponding to the reverse reactions of polysulfides back to the sulfide.[41] The negligible position shift of both oxidation and reduction peaks of the CV curves and small overpotential between the cathodic and anodic processes imply that this electrode can operate with an excellent reversibility, good stability, and fast kinetics. Furthermore, the sharp reduction and oxidation peaks are clear evidence of high reactivity of S contained in the Fe_xS@N-GE-CNTs hybrids. **Figure 6b** shows typical galvanostatic charge/discharge curves at 0.2 C within a voltage window of 1.7 - 2.7 V. The discharge and charge profiles clearly show two plateaus, which are consistent with the CV results. The plateau between 2.5 - 2.1 V in charging profiles and 2.1 - 2.0 V in discharge profiles are related to the formation of long-chain lithium polysulfides and short-chain lithium polysulfides, respectively. The S@Fe_xS@N-GE-CNTs hybrid electrode delivered a high initial discharge specific capacity of 1224 mA h g^{-1} (with the capacity calculation based on the mass of sulfur). After 20 cycles, the electrode maintained a capacity of 1117 mA h g^{-1}. After 60 cycles, the electrode still retained a high discharge capacity of 1071 mA h g^{-1}. Even after 100 cycles, the electrode had nearly 91 % capacity retention (ca. 1014 mA

h g^{-1}). **Figure 6**c shows the cycling stability and Coulombic efficiency of the cells at different rates. At 0.5 C, the initial discharge capacity was 1040 mA h g^{-1}, with 759 mA h g^{-1} being sustained after 100 cycles and representing minor capacity loss of 0.27 % per cycle. The S@Fe_xS@N-GE-CNTs hybrid electrode also showed high Coulombic efficiencies at both 0.2 and 0.5 C. **Figure 6**d compares the initial galvanostatic charge and discharge profiles at different rates (0.5, 1, 2, 5 and 10 C). Although the overpotentials between charge and discharge processes gradually increase along with increased current densities, they all preserved the typical plateaus, indicating the stability at different rates. The electrodes exhibited high initial capacities of 844, 712, 458, and 220 mA h g^{-1} at 1, 2, 5 and 10 C rates, respectively. Furthermore, the electrodes demonstrated superior cycling performances at high rates of 1, 2 and 5 C (**Figure 7a**). Reversible capacities of 629, 495, and 332 mA h g^{-1} were retained after 1000 cycles at 1, 2, and 5 C rates, respectively. Surprisingly, the electrodes also show superior cycling performances at high current rate of 10 C (10 minutes to fully charge and discharge, **Figure 7b**). The samples still delivered exceptional reversible capacities of 158 and 128 mA h g^{-1}, after 1000 and 2000 cycles, respectively, with a degradation rate of 0.037% /cycle. Moreover, the high Coulombic efficiencies at high rates can be maintained after thousands of cycles. This indicates that the electrode can minimize processes such as loss of electrical contact of Li_2S or sulfur with the conductive host caused by volume changes or the 'shuttle reaction' caused by the dissolution of polysulfides. **Figure 7c** shows the results of S@Fe_xS@N-GE-CNTs hybrid electrode cycled at varied current rates. During the charge/discharge processes, the electrode was cycled from low current rates to high current rates and then returned to low rates. The results show that at lower current rates, high discharge capacity was obtained. Although the capacity decreased with increasing current rate, the electrodes still maintained high discharge capacities. Furthermore, a capacity of 1135 mA h g^{-1} was recovered when the current rate was reversed back to 0.2 C. This indicates that the S@Fe_xS@N-GE-CNTs hybrids electrode can tolerate varied current rates and has excellent rate capability and stability.

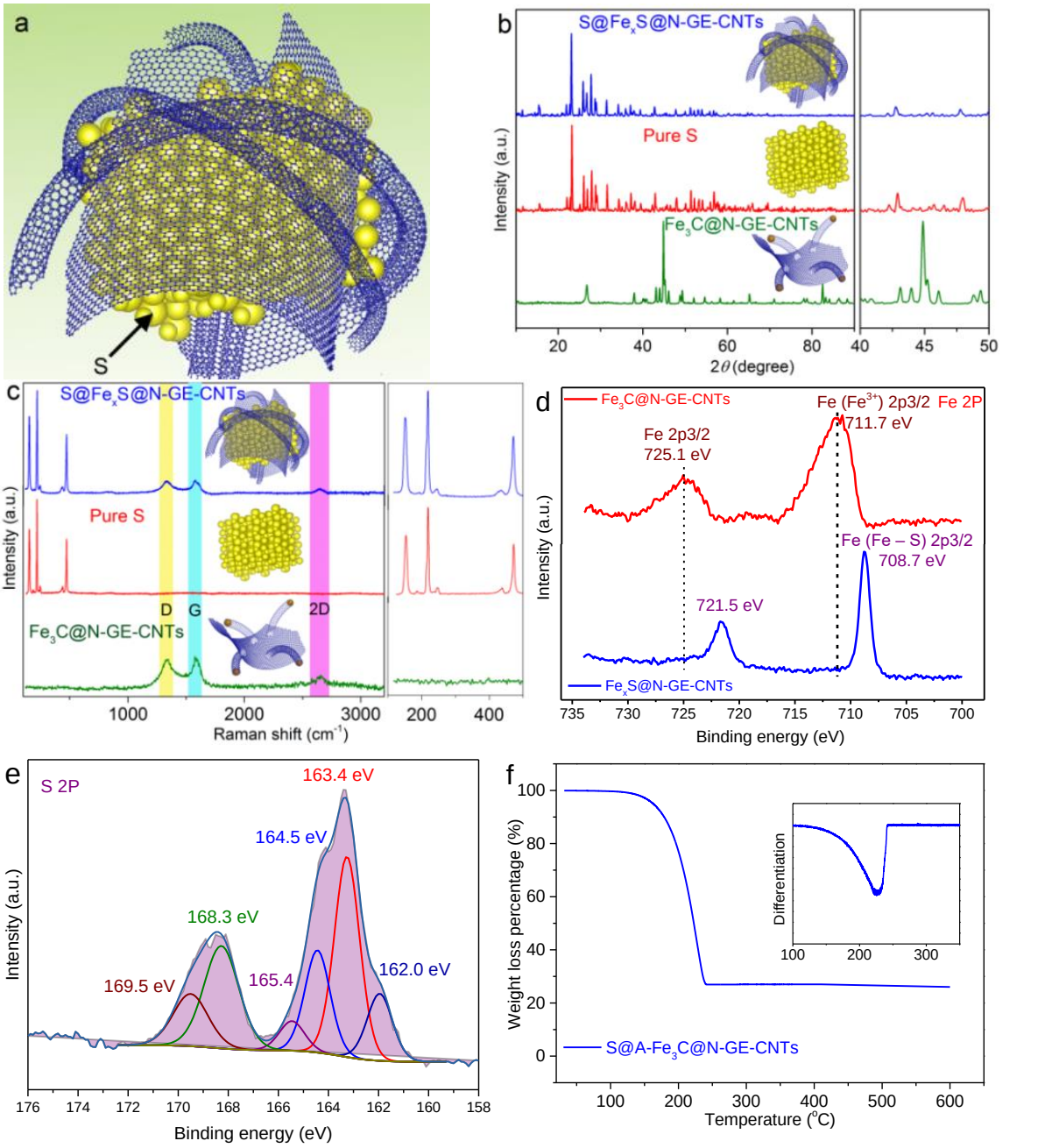

Figure 5. (a) Schematic diagram of S@FexS@N-GE-CNTs hybrids. (b) XRD patterns. (c) Raman spectra of S@FexS@N-GE-CNTs hybrids, pure S and Fe3C@N-GE-CNTs hybrids. (d) XPS of iron 2p of Fe3C@N-GE-CNTs and FexS@N-GE-CNTs hybrids. (e) XPS of sulfur 2p of FexS@N-GE-CNTs hybrids. (f) TGA curves of S@FexS@N-GE-CNTs hybrids. Inset is the corresponding first derivative of temperature *vs*. time.

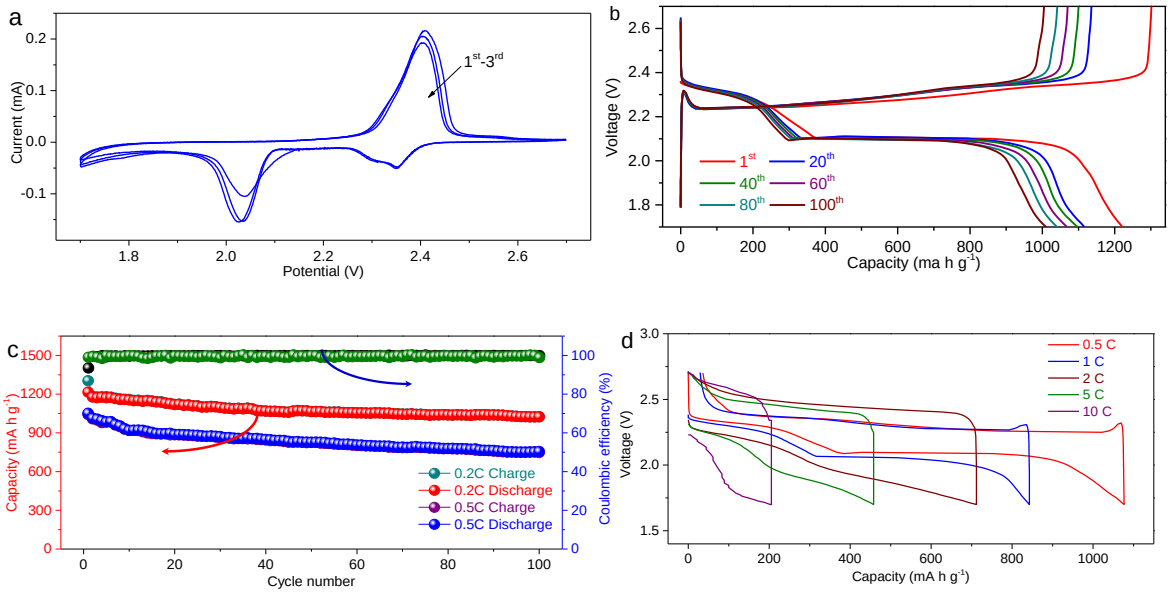

Figure 6. (a) 1st – 3rd CV curves of S@ Fe_xS@ N-GE-CNTs hybrids at a scan rate of 0.1 mV s^{-1}. (b) Typical charge and discharge profiles of S@ Fe_xS@ N-GE-CNTs hybrids for the 1st, 20th, 40th, 60th, 80th, and 100th cycles at 0.2 C. (c) Cycling performances and Coulombic efficiencies of S@ Fe_xS@ N-GE-CNTs hybrids at 0.2 and 0.5 C rates. (d) The 1st cycle charge and discharge profiles of S@ Fe_xS@ N-GE-CNTs hybrids at 0.5, 1, 2, 5, and 10 C rates.

The electrochemical performance of Li-S batteries made when RGO-CNTs composites were melted with S (blue curve in **Figure 3**f, **Figure S13,** and **S14**, SI) was also evaluated (**Figure S15**, SI). Although high initial discharge capacities were obtained at current rates of 0.2 and 0.5 C (1045 and 1004 mA h g^{-1}, respectively, **Figure S15**a and b, SI), the values quickly dropped to less than 400 mA h g^{-1} after 100 cycles and less than 300 mA h g^{-1} after 200 cycles (**Figure S15**c and d, SI). In contrast the S@ Fe_xS@ N-GE-CNTs hybrids demonstrated outstanding electrochemical properties for Li-S batteries, which can be ascribed to the incorporation of nitrogen atoms into the hierarchical 2D graphene and 1D carbon nanotube hybrids, inducing more active defect sites on the interface and edges, and therefore improving the affinity between sulfur, polysulfides and the nitrogen-doped carbon scaffolds.[22b,22c,42] Furthermore, the good conductivity of 2D graphene and 1D carbon nanotube ar-

chitecture also contributes to improve overall electron conductivity. The rigid 2D matrix can prevent the dissolution of polysulfides, minimize the shuttle effect, thus, solving the polysulfide dissolution problem and improving the cycling performance. The 3D interconnected porous space leads to the easy penetration and diffusion of electrolytes. It can be seen that there is no obvious change on the A.C. impedance of S@ Fe_xS@ N-GE-CNTs hybrids before and after cycling test (**Figure S16**, SI).

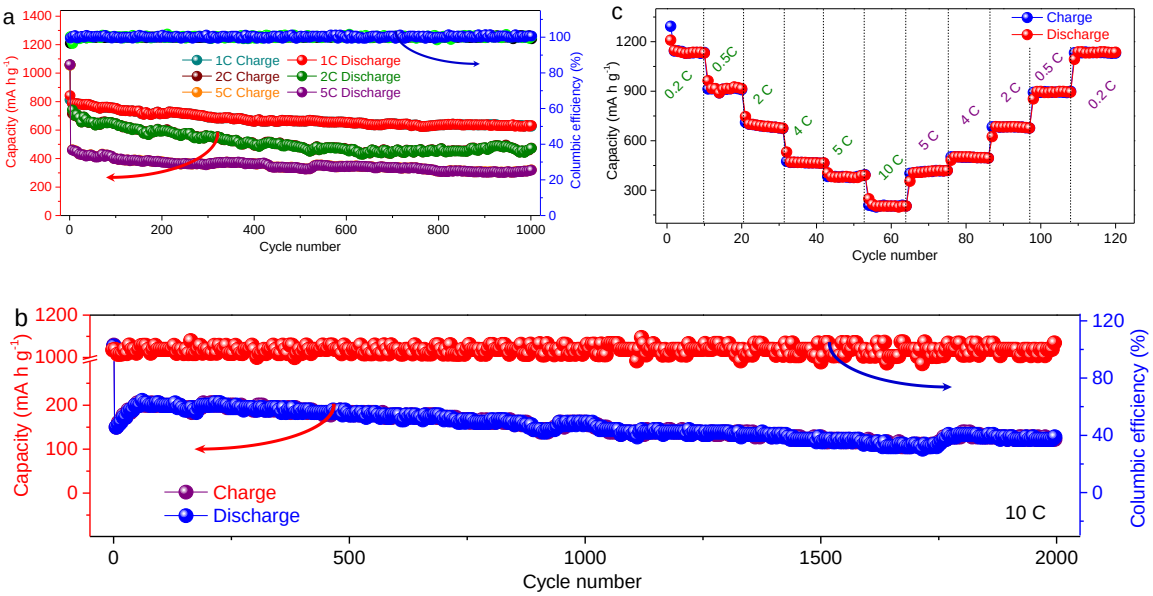

Figure 7. (a) Cycling performances and Coulombic efficiencies of S@ Fe_xS@ N-GE-CNTs hybrids at 1, 2, and 5 C rates. The 1st cycle was tested at 0.5 C. (b) Cycling performance and Coulombic efficiency of S@ Fe_xS@ N-GE-CNTs hybrids at 10 C. The 1st cycle was tested at 0.5 C. (c) Cycling performance of S@ Fe_xS@ N-GE-CNTs hybrids at varied current rates (0.2, 0.5, 2, 4, 5, and 10 C).

To examine the lithium polysulfide interaction with Fe_xS@ N-GE-CNTs hybrids, the *ex-situ* Raman spectra of the S@ Fe_xS@ N-GE-CNTs hybrids after 1000 cycles were collected (**Figure 8**). It can be seen that besides the D and G bonds, corresponding to the N-GE-CNTs hybrids, the peaks at 126 and 748 cm^{-1} are the vibrations from the lithium nitrate ($LiNO_3$) and lithium bis-(trifluoromethanesulfonyl)imide (LiTFSI) additives in the electrolyte, respectively. The peaks at 331, 1149, and 1247 cm^{-1} correspond to the DME and DIOX electrolyte, the peaks at 155, 192, and

397 cm^{-1} derive from the S_8^-, and the peaks at 280 and 552 cm^{-1} originate from the S_6^-.[37] Therefore, this clearly confirmed that polysulfides (S_8^-, S_6^-) were entrapped on the cathode. This benefits the cycling performance of the electrode. Therefore, the hybrid material functions as a redox shuttle to catenate and bind polysulfides, and convert them to insoluble lithium sulfide. On the contrary, no obvious new peaks can be observed in the S@RGO-CNTs composites after 1000 cycles (**Figure S17**, SI). This indicates that the lithium polysulfides in the S@RGO-CNTs composites were dissolved in the electrolyte. For this reason, the cycling performance of S@RGO-CNTs composites is not as good as that of the S@Fe_xS@N-GE-CNTs electrode. The N-GE-CNT hybrid structure preventing polysulfide dissolution could be ascribed to the unique 3D hierarchical architecture bonded by 1D CNT and 2D GE, in which the high surface area and mesopores can prevent polysulfides from dissolving in the electrolyte.[2] Furthermore, the nitrogen doped sp^2 carbons with enhanced interfacial affinity also contributed to confine polysulfide dissolution,[42] benefiting the enhanced cycling and rate performances for Li-S batteries. This is because nitrogen bears five valence electrons which induces a shift in the Fermi level to the conducting band,[22] significantly improving electrochemical performance.[10a, 43] We conducted XPS measurement to confirm the interaction between polysulfides and N-GE-CNT hybrid. As shown in Figure 8b, the Li 1s XPS spectrum of electrode after discharging to 2.0 V, exhibits a single asymmetric peak at around 56.0 eV which can be fitted to two peaks at position of 55.6 and 57.2 eV, respectively. The former corresponds to the Li-S binding energy resulting from polysulfides. The later with a +1.2 eV shift can be attributed to the Li in the polysulfides interacting with doped N (Li–N). Because normally, the Li 1s XPS spectrum only show the symmetric peak around 56 eV, this result is consistent with the previous report.[23] Furthermore, the corresponding N 1s XPS spectrum shows the peaks shifts of the graphitic N and pyrrolic N due to the interaction between the N and Li (**Figure S18**, SI), confirming that nitrogen doped GE-CNT hybrid can trap the polysulfides and contribute to confine polysulfide dissolution.

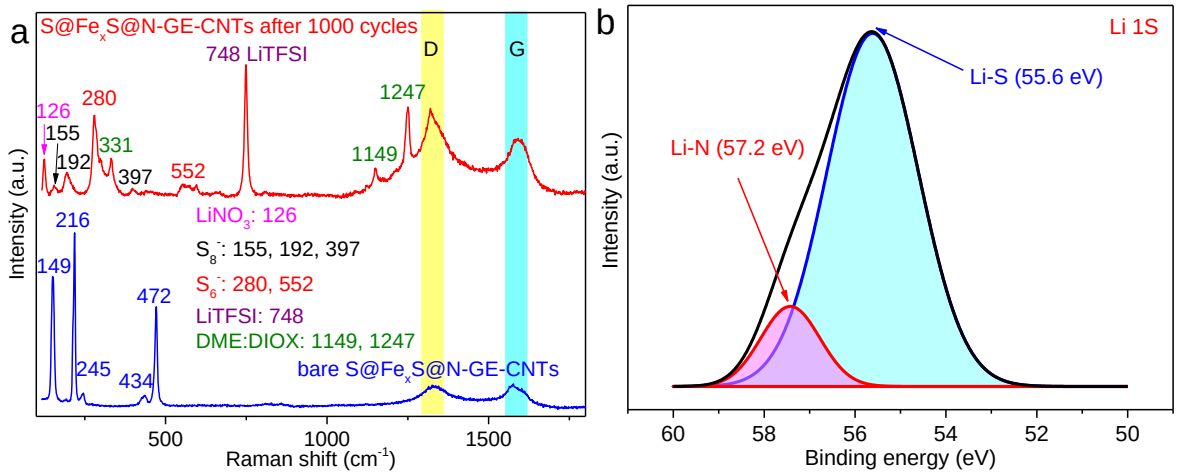

Figure 8. (a) *Ex-situ* Raman spectra of bare S@Fe_xS@N-GE-CNTs hybrids and the electrode after 1000 cycles at 1 C and discharge down to 2.0 V. (b) XPS of Li1s of the electrode after discharge down to 2.0 V.

Conclusion

We discovered a facile one-step method to synthesize 3D nitrogen doped graphene - carbon nanotube hybrids (Fe_3C@N-GE-CNTs) using low-cost precursors. It was observed by means of FESEM, TEM, XRD, Raman spectra, AFM, and isothermal analyses that 2D graphene and 1D carbon nanotubes were bonded seamlessly during the growth stage, which is an ideal architecture as a scaffold to accommodate sulfur for Li-S batteries. After conversion to Fe_xS@N-GE-CNTs, the hybrid material demonstrated a high reversible capacity of 1221 mA h g^{-1}, high rate capability (844, 712, 458, and 220 mA h g^{-1} at 1, 2, 5 and 10 C, respectively), and excellent cycling stability at high rates (332 and 158 mA h g^{-1} at 5 and 10 C after 1000 cycles). The enhanced electrochemical performance can be attributed to the unique architecture combining 2D graphene and 1D carbon nanotubes, which improves the electron conductivity, prevents the dissolution of polysulfides, and minimizes the shuttle effect. The 3D interconnected porous spaces also facilitate the penetration and diffusion of electrolytes. Furthermore, the doped nitrogen introduces more defects and active sites to

the carbon framework and effectively traps lithium polysulfides on electroactive sites within the cathode. This strategy could open a new avenue for developing high performance Li-S batteries.

ACKNOWLEDGMENT

This original research was supported by the Commonwealth of Australia, the Australian Renewable Energy Agency (ARENA) and UTS Early Career Researcher Grants through the ARC Future Fellowship Project (FT1101000800), ARENA 2014/RND106 and ECRGS PRO16-1304. This research used the TEM facility located at the UOW Electron Microscopy Centre, which was funded by an Australian Research Council (ARC) Linkage, Infrastructure, Equipment and Facilities (LIEF) grant (LE0237478). The authors acknowledge the assistance of Dr David Mitchell for EELS analysis.

Received: ((will be filled in by the editorial staff))
Revised: ((will be filled in by the editorial staff))
Published online: ((will be filled in by the editorial staff))

References

[1] a) G. Zhou, S. Pei, L. Li, D.-W. Wang, S. Wang, K. Huang, L.-C. Yin, F. Li, H.-M. Cheng, *Adv. Mater.* **2014**, *26*, 625; b) Y.-X. Yin, S. Xin, Y.-G. Guo, L.-J. Wan, *Angew. Chem. Inter. Ed.* **2013**, *52*, 13186.

[2] L. Yuan, H. Yuan, X. Qiu, L. Chen, W. Zhu, *J. Power Sources* **2009**, *189*, 1141.

[3] M. Seredych, R. Chen, T. J. Bandosz, *Carbon* **2012**, *50*, 4144.

[4] A. D. McNaught, A. Wilkinson, *Compendium of Chemical Terminology*, Blackwell Scientific Publications, Oxford 1997.

[5] J. Kong, N. R. Franklin, C. Zhou, M. G. Chapline, S. Peng, K. Cho, H. Dai, *Science* **2000**, *287*, 622.

[6] S. W. Lee, N. Yabuuchi, B. M. Gallant, S. Chen, B.-S. Kim, P. T. Hammond, Y. Shao-Horn, *Nat. Nanotech.* **2010**, *5*, 531.

[7] G. W. Rogers, J. Z. Liu, *J. Am. Chem. Soc.* **2011**, *133*, 10858.

[8] X. Wang, L. Zhi, K. Müllen, *Nano Lett.* **2008**, *8*, 323.

[9] J. J. Yoo, K. Balakrishnan, J. Huang, V. Meunier, B. G. Sumpter, A. Srivastava, M. Conway, A. L. Mohana Reddy, J. Yu, R. Vajtai, *Nano Lett.* **2011**, *11*, 1423.

[10] a) Z.-S. Wu, W. Ren, L. Xu, F. Li, H.-M. Cheng, *ACS Nano* **2011**, *5*, 5463; b) L.-H. Hu, F.-Y. Wu, C.-T. Lin, A. N. Khlobystov, L.-J. Li, *Nat. Commun.* **2013**, *4*, 1687.

[11] a) G. Zhou, D.-W. Wang, F. Li, P.-X. Hou, L. Yin, C. Liu, G. Q. M. Lu, I. R. Gentle, H.-M. Cheng, *Energy Environ. Sci.* **2012**, *5*, 8901; b) S. Dörfler, M. Hagen, H. Althues, J. Tübke, S. Kaskel, M. J. Hoffmann, *Chem. Commun.* **2012**, *48*, 4097.

[12] H. Wang, Y. Yang, Y. Liang, J. T. Robinson, Y. Li, A. Jackson, Y. Cui, H. Dai, *Nano Lett.* **2011**, *11*, 2644.

[13] C. Zhang, W. Lv, W. Zhang, X. Zheng, M.-B. Wu, W. Wei, Y. Tao, Z. Li, Q.-H. Yang, *Adv. Energy Mater.* **2014**, *4*, n/a.

[14] Q. Sun, X. Fang, W. Weng, J. Deng, P. Chen, J. Ren, G. Guan, M. Wang, H. Peng, *Angew. Chem.* **2015**, *127*, 10685.

[15] X. Liang, C. Hart, Q. Pang, A. Garsuch, T. Weiss, L. F. Nazar, *Nat. Commun.* **2015**, *6*.

[16] a) Y. Zhu, L. Li, C. Zhang, G. Casillas, Z. Sun, Z. Yan, G. Ruan, Z. Peng, A.-R. O. Raji, C. Kittrell, *Nat. Commun.* **2012**, *3*, 1225; b) M. K. Shin, B. Lee, S. H. Kim, J. A. Lee, G. M. Spinks, S. Gambhir, G. G. Wallace, M. E. Kozlov, R. H. Baughman, S. J. Kim, *Nat. Commun.* **2012**, *3*, 650; c) H. T. Chung, J. H. Won, P. Zelenay, *Nat. Commun.* **2013**, *4*, 1922.

[17] X. Fang, H. Peng, *Small* **2015**, *11*, 1488.

[18] C. Tang, Q. Zhang, M. Q. Zhao, J. Q. Huang, X. B. Cheng, G. L. Tian, H. J. Peng, F. Wei, *Adv. Mater.* **2014**, *26*, 6100.

[19] M.-Q. Zhao, X.-F. Liu, Q. Zhang, G.-L. Tian, J.-Q. Huang, W. Zhu, F. Wei, *ACS Nano* **2012**, *6*, 10759.

[20] V. C. Tung, L.-M. Chen, M. J. Allen, J. K. Wassei, K. Nelson, R. B. Kaner, Y. Yang, *Nano Lett.* **2009**, *9*, 1949.

[21] P. Chen, T.-Y. Xiao, Y.-H. Qian, S.-S. Li, S.-H. Yu, *Adv. Mater.* **2013**, *25*, 3192.

[22] a) L. Qie, W. M. Chen, Z. H. Wang, Q. G. Shao, X. Li, L. X. Yuan, X. L. Hu, W. X. Zhang, Y. H. Huang, *Adv. Mater.* **2012**, *24*, 2047; b) W. H. Shin, H. M. Jeong, B. G. Kim, J. K. Kang, J. W. Choi, *Nano Lett.* **2012**, *12*, 2283; c) J. Song, T. Xu, M. L. Gordin, P. Zhu, D. Lv, Y. B. Jiang, Y. Chen, Y. Duan, D. Wang, *Adv. Funct. Mater.* **2014**, *24*, 1243.

[23] Q. Pang, J. Tang, H. Huang, X. Liang, C. Hart, K. C. Tam, L. F. Nazar, *Adv. Mater.* **2015**, *27*, 6021.

[24] S. Chen, J. Bi, Y. Zhao, L. Yang, C. Zhang, Y. Ma, Q. Wu, X. Wang, Z. Hu, *Adv. Mater.* **2012**, *24*, 5593.

[25] Y. Zhao, R. Nakamura, K. Kamiya, S. Nakanishi, K. Hashimoto, *Nat. Commun.* **2013**, *4*.

[26] X. Ji, K. T. Lee, L. F. Nazar, *Nat. Mater.* **2009**, *8*, 500.

[27] J. Qian, M. Zhou, Y. Cao, X. Ai, H. Yang, *Adv. Energy Mater.* **2012**, *2*, 410.

[28] a) D. Amara, S. Margel, *Colloid Polym. Sci.* **2013**, *291*, 2121; b) J. Su, Y. Gao, R. Che, *Mater. Lett.* **2010**, *64*, 680.

[29] W. Yang, X. Liu, X. Yue, J. Jia, S. Guo, *J. Am. Chem. Soc.* **2015**, *137*, 1436.

[30] Y. Hou, T. Huang, Z. Wen, S. Mao, S. Cui, J. Chen, *Adv. Energy Mater.* **2014**, *4*.

[31] a) F. D. Novaes, R. Rurali, P. Ordejón, *ACS Nano* **2010**, *4*, 7596; b) G. K. Dimitrakakis, E. Tylianakis, G. E. Froudakis, *Nano Lett.* **2008**, *8*, 3166; c) S. Hofmann, R. Sharma, C. Ducati, G. Du, C. Mattevi, C. Cepek, M. Cantoro, S. Pisana, A. Parvez, F. Cervantes-Sodi, *Nano Lett.* **2007**, *7*, 602.

[32] S. Helveg, C. Lopez-Cartes, J. Sehested, P. L. Hansen, B. S. Clausen, J. R. Rostrup-Nielsen, F. Abild-Pedersen, J. K. Nørskov, *Nature* **2004**, *427*, 426.

[33] S. Reich, L. Li, J. Robertson, *Phys. Rev. B* **2005**, *72*, 165423.

[34] L. Guan, J. Li, *J. Phys. Chem. C* **2009**, *113*, 7481.

[35] Y.-Q. Zhang, D.-K. Ma, Y. Zhuang, X. Zhang, W. Chen, L.-L. Hong, Q.-X. Yan, K. Yu, S.-M. Huang, *J. Mater. Chem.* **2012**, *22*, 16714.

[36] J. Niu, H. Gao, L. Wang, S. Xin, G. Zhang, Q. Wang, L. Guo, W. Liu, X. Gao, Y. Wang, *New J. Chem.* **2014**, *38*, 1522.

[37] M. Hagen, P. Schiffels, M. Hammer, S. Dörfler, J. Tübke, M. Hoffmann, H. Althues, S. Kaskel, *J. Electrochem. Soc.* **2013**, *160*, A1205.

[38] S. Boursiquot, M. Mullet, J.-J. Ehrhardt, *Surf. Interface Anal.* **2002**, *34*, 293.

[39] D. Mandrino, *Mater. Tech.* **2011**, *45*, 325.

[40] a) L. Xiao, Y. Cao, J. Xiao, B. Schwenzer, M. H. Engelhard, L. V. Saraf, Z. Nie, G. J. Exarhos, J. Liu, *Adv. Mater.* **2012**, *24*, 1176; b) M.-K. Song, Y. Zhang, E. J. Cairns, *Nano Lett.* **2013**, *13*, 5891; c) M.-K. Song, E. J. Cairns, Y. Zhang, *Nanoscale* **2013**, *5*, 2186.

[41] J. Nelson, S. Misra, Y. Yang, A. Jackson, Y. Liu, H. Wang, H. Dai, J. C. Andrews, Y. Cui, M. F. Toney, *J. Am. Chem. Soc.* **2012**, *134*, 6337.

[42] C. Tang, Q. Zhang, M. Q. Zhao, J. Q. Huang, X. B. Cheng, G. L. Tian, H. J. Peng, F. Wei, *Adv. Mater.* **2014**, *26*, 6100.

[43] P. Chen, T. Y. Xiao, Y. H. Qian, S. S. Li, S. H. Yu, *Adv. Mater.* **2013**, *25*, 3192.

Herein, we report a Fe_3C@nitrogen-doped graphene - carbon nanotube (Fe_3C@N-GE-CNTs) hybrid material for sulphur storage in lithium-sulfur (Li-S) batteries. The new hybrid material was prepared by a one-step pyrolysis process using dehydrated sodium ferrocyanide as a precursor. Lithium-sulfur batteries made with these cathodes demonstrated outstanding electrochemical performances.

Keywords: One step synthesis, Fe_3C@nitrogen-doped graphene - carbon nanotube hybrid materials, lithium-sulphur batteries

Dawei Su, Michael Cortie, and Guoxiu Wang *

Fabrication of N-doped graphene-carbon nanotube hybrids from Prussian blue for lithium-sulfur batteries

TOC